*applied sciences*

MDPI

*Article*

# Impact Airflow Evolution Induced by Hard Roof Collapse in Contiguous Seams and the Forced Ventilation Technology

**Haiyang Wang [1,2], Chunxin Zhai [2,*], Feng Yang [1,*], Yanmin Zhou [2] and Yin Yang [2]**

[1] Sichuan Highway Planning, Survey, Design and Research Institute Ltd., Chengdu 610031, China
[2] School of Civil Engineering, Chongqing Jiaotong University, Chongqing 400074, China
* Correspondence: zhaichunxin@yeah.net (C.Z.); yangfeng1991@126.com (F.Y.)

**Abstract**

In contiguous seam mining, the sudden large-scale collapse of a hard roof in an overlying goaf generates violent impact airflow, driving hazardous gases into the underlying working face and seriously threatening production safety. However, quantitative analysis of airflow responses under such transient impacts is rare for conventional exhaust ventilation systems, and proactive control strategies remain lacking. This study hypothesized that replacing exhaust ventilation with a forced ventilation system builds a sufficient counter-pressure gradient across the working face to block the downward migration of hazardous gases. Taking the Longhua Coal Mine as the engineering background, this study combines a theoretical velocity model of roof-collapse-induced impact airflow with numerical simulations and subsequently implements a forced ventilation system on site. Results show that under exhaust ventilation, roof collapse greatly intensifies air leakage in the goaf, causing the CO concentration at the return corner to spike to 5000 ppm within only 0.2 s. In contrast, the field-deployed forced ventilation system effectively suppresses this impact: by keeping the pressure difference across the air regulator within 338–417 Pa, the CO concentration drops from 36 ppm to below 15 ppm. Complemented by a real-time monitoring system for goaf pressure surges and hazardous gases, this strategy successfully shifts disaster control from passive ventilation to active aerodynamic suppression. This study provides a robust theoretical foundation and practical engineering reference for disaster prevention in contiguous seam mining.

**Keywords:** contiguous seams; mining under a goaf of fire area; impact airflow; harmful gases inrush; forced ventilation system



Academic Editor:
Nikolaos Koukouzas

Received: 22 April 2026
Revised: 18 May 2026
Accepted: 20 May 2026
Published: 22 May 2026



## 1. Introduction

The coal seams in northwest China (such as Inner Mongolia and northern Shaanxi) are generally characterized by shallow burial, thin bedrock, and relatively simple geological conditions [1,2]. In the 1980s, limited by the backward domestic coal mining mechanization technology, the mining area in this region widely used room and pillar mining [3,4]. In this method, only the goaf is opened while the coal pillar is reserved to support the roof [5,6]. Although this method is conducive to maintaining the relative stability of the goaf roof and reducing the occurrence of roof collapse and roadway-side accidents, it also leads to a low coal recovery rate and a large number of coal pillars and unmined coal bodies (referred to as residual coal) left in the goaf. Once the spontaneous combustion of residual coal occurs, it is easy to form a large area of spontaneous combustion in the goaf, which is difficult to control [7,8].

Large-scale spontaneous combustion of the coal in the goaf typically creates a relatively closed environment with restricted oxygen supply channels [9,10]. The limited ventilation and oxygen availability result in incomplete combustion of residual coal, generating substantial quantities of toxic gases such as CO and causing flooding in fire areas [11]. Concurrently, when the upper hard roof undergoes large-scale collapse, it may trigger a strong impact air disaster. The impact airflow not only triggers floor rockbursts but also causes abnormal migration of accumulated harmful gases from the goaf into working faces and roadways, posing significant threats to safe mining operations in underlying coal seams [12]. Consequently, in contiguous seam mining, a comprehensive investigation of the evolutionary mechanisms of impact airflow, abnormal gas emission patterns, and associated ventilation control measures induced by hard roof collapse in the overlying goaf is of paramount theoretical and practical significance for mitigating accident consequences and ensuring personnel safety.

Extensive research on coal mine impact airflow has been conducted by both domestic and international scholars. Findings indicate that coal and gas outbursts, gas explosions, and floor rockbursts are the primary causes of impact airflow. Owing to their immense destructive power and sudden onset, such events are extremely difficult to monitor in the field. Consequently, experimental and numerical simulations have become the most effective methods for investigating the impact airflow. Wang et al. [13] analyzed the formation mechanisms of impact airflow and identified their attenuation characteristics using a geometric model of a straight roadway. Cheng et al. [14] developed formation and flow models of impact airflow through T-shaped roadway outburst experiments, characterized the dynamic evolution of impact force during the two-phase flow stage, and revealed the secondary acceleration phenomenon of impact airflow in a T-shaped roadway. Xu et al. [15] examined coal seam in situ stress and gas pressure variations and impact airflow movement characteristics in coal seams by integrating formation and migration models of impact airflow with coal mine dynamic disaster simulation. Nevertheless, current studies have yet to achieve complete prevention of impact airflow disasters.

As coal mining extends to greater depths, geological conditions become increasingly complex, rendering the control of impact airflow more challenging. Consequently, numerous scholars have investigated disaster initiation mechanisms and impact airflow migration characteristics. Wang et al. [16] analyzed the formation processes of impact airflow and gas outbursts, employing a numerical model of a right-angle cross roadway to determine propagation and attenuation patterns of impact airflow and gas migration. Sun et al. [17] utilized a coal–gas outburst simulation device to reproduce the two-phase flow pattern of coal-gas mixtures in roadway networks, using coal samples from the outburst coal seam in Yuyang Coal Mine, Chongqing. Jin et al. [18] and A. Zhou et al. [19] investigated the influence of gas desorption on impact airflow propagation in roadways using novel testing devices. Based on the influence factors of gas explosion overpressure and impact airflow velocity in the roadway with propagation distance attenuation, Cheng et al. [20] established a dimensionless model of the propagation law. Yang et al. [21] employed a self-developed outburst simulation system to examine the evolution and characteristics of impact airflow induced by coal and gas outbursts. A. Zhou et al. [10] implemented three-dimensional numerical simulations to analyze ventilation airflow disturbances caused by impact airflow. Liu [22] utilized a horizontal pipe coal dust explosion experimental device coupled with a lignite explosion propagation model to investigate the impact airflow propagation characteristics. Wang et al. used a self-developed outburst testing device to simulate conditions at windbreak door bases of varying dimensions. B. Zhou et al. [23] examined the dynamic relationship between gas pressure and outburst intensity through experimental analysis, exploring the disaster evolution mechanism of impact forces under different gas pressure conditions.

Despite these advancements, current research on impact airflow disasters in coal mines predominantly focuses on triggers such as gas explosions and coal-gas outbursts, with few studies examining those induced by large-scale hard roof collapses. Such disasters are even more rarely reported under contiguous seam conditions, where a hard roof collapses in the overlying goaf of an active working face. For example, the primary mining seam at the Sunjiacha Longhua Coal Mine is the $3^{-1}$ seam, while the overlying $2^{-2}$ seam was historically extracted by small-scale mines using the room and pillar method. This earlier method resulted in two major issues: (1) the formation of a large suspended hard roof; and (2) prolonged air leakage and oxygen ingress, which led to extensive spontaneous combustion within the $2^{-2}$ seam goaf. Given that the $2^{-2}$ and $3^{-1}$ seams are contiguous, separated by only 30–40 m. In particular, a large volume of toxic and hazardous gases has accumulated in the upper fire area above the 30110 working face of the $3^{-1}$ seam. Monitoring through borehole sampling in the main recovery roadway and secondary main gateroad revealed that the average CO concentration in the $2^{-2}$ seam goaf reached approximately 10,000 ppm, with peak values up to 16,000 ppm. During mining, repeated abnormal CO emissions were recorded, severely disrupting operations at the working face and posing serious safety hazards to production. The geographical location of this mine is shown in Figure 1.

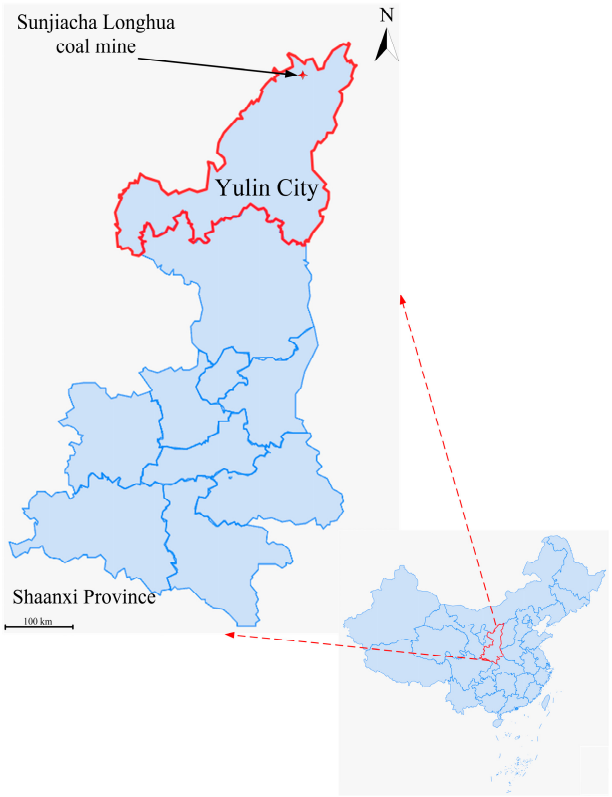


**Figure 1.** Mine location.

Few studies have examined impact airflow disasters triggered by hard-roof collapse in the overlying goaf of contiguous seams, and the combination of theoretical modeling, numerical simulation, and field ventilation retrofitting has rarely been attempted. This study addresses this gap by coupling numerical simulations of roof-collapse-induced gas inrush with a field-implemented pressure-balancing ventilation system, thereby developing an integrated proactive prevention strategy. We hypothesize that switching from conventional exhaust ventilation to a purpose-designed forced ventilation system generates a counter-pressure gradient sufficient to suppress the abnormal downward influx of CO during hard-roof collapse.

To test this hypothesis, the specific objectives are to: (1) establish a theoretical velocity model to quantify the energy evolution and principal controlling factors induced by roof collapse; (2) use Fluent numerical simulations to reveal the evolution of the impact airflow and the spatiotemporal distribution of CO influx under the exhaust ventilation mode; and (3) design, implement, and evaluate a forced ventilation system at the 30110 working face and develop a corresponding real-time monitoring and early-warning system. These results are intended to provide a theoretical basis and engineering reference for safe mining and disaster prevention in the underlying working faces of contiguous seams.

## 2. Analysis of the Formation Process and Influencing Factors of Impact Air Disasters

### *2.1. Process Analysis of the Impact Airflow Induced by the Hard Roof Collapse*

After the large-scale collapse of the hard roof, the collapsed rock mass rapidly moves into the goaf in a non-integral movement, violently compressing the gas stored within the goaf. Given the extremely short duration of roof collapse and the finite propagation speed of the pressure waves generated by gas compression, the transmission of compressed gas inevitably lags behind the instantaneous compression induced by the rockfall. Consequently, the gas pressure in the goaf rises sharply within a short timescale. Once the accumulated pressure exceeds the resistance, the high-pressure gas generates impact airflow, surging toward adjacent working faces, roadways, and other low-pressure zones, as illustrated in Figure 2.

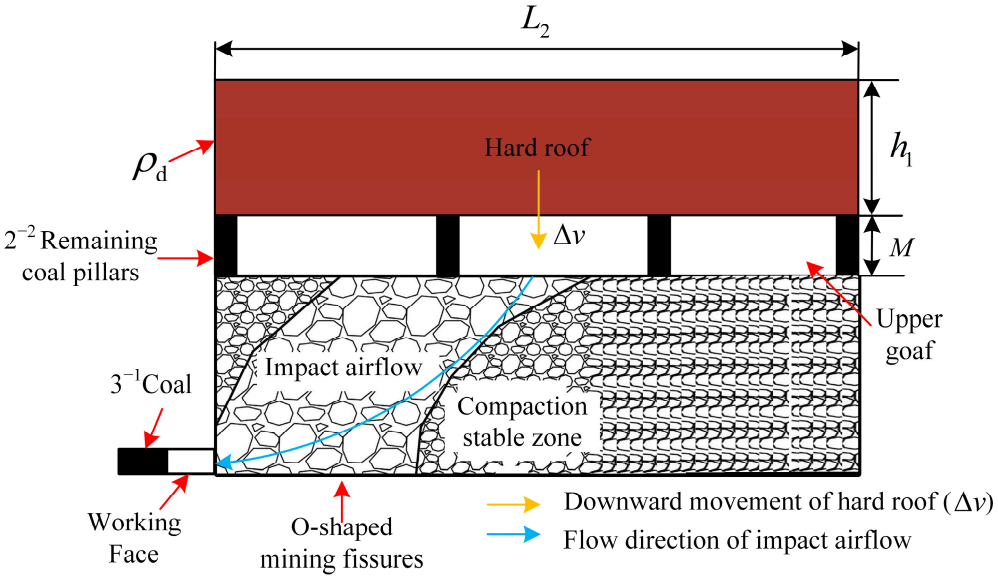


**Figure 2.** Forming process of impact gas flow.

The formation process of impact airflow induced by hard roof collapse can be divided into three stages: (1) Gas compression and pressure buildup stage: when a large section of the roof collapses instantaneously, the fragmented rock mass rapidly occupies the space of the lower goaf, violently compressing the gas and causing a sharp pressure rise. During this stage, a small portion of the high-pressure gas might migrate into the adjacent fissured rock mass. (2) Impact airflow formation and rock body impact stage: Once the compressed gas pressure becomes sufficient to overcome the resistance of the fissured rock mass channels, the high-pressure gas rapidly surges into the lower fissured zones. This sudden inflow generates an impact wave, which strikes collapsed fragments or partially failed rock structures, releasing substantial kinetic energy. (3) Impact airflow release and working face inrush stage: the high-pressure gas breaks through the fissured zones and inrushes into the coal mining working face and connected roadways. The impact airflow, carrying potentially harmful gases and dust,

propagates rapidly through the roadways, posing a direct threat to the operators, equipment, and facilities until the release process is completed.

### 2.2. Theoretical Modeling of Impact Airflow Velocity

Under close-distance coal seam mining, the collapse process of the large hard roof above the working face is influenced by many random factors, including the collapsed area, collapse duration, interval between initial and subsequent collapse events, and the extent of the roof involved in later collapses. In this study, only the case of a single, instantaneous large-area roof collapse is considered.

During the propagation of impact airflow induced by hard roof collapse, the gas temperature will be influenced by formation temperature, friction, and air compression, among other factors, resulting in minor changes. However, its impact on the main transport and propagation characteristics of the impact airflow is relatively limited. Therefore, the airflow in the goaf and roadway can be reasonably approximated as adiabatic, inviscid, and compressible flow. Furthermore, local gas temperature changes caused by the work performed during roof collapse, as well as potential upward flows induced by temperature differences in the goaf, are neglected.

To simplify the analytical model, the following assumptions are made in this study:

(1) Because the evolution of impact airflow occurs within an extremely short time and gases have weak heat transfer capacity, heat exchange with the surrounding rock and the external environment can be neglected. Consequently, the gas flow within the goaf is treated as an isothermal process (i.e., temperature change $\Delta T = 0$);

(2) The roof of the $2^{-2}$ coal seam in Longhua Coal Mine consists mainly of sandstone. When the room-and-pillar goaf becomes unstable, the roof undergoes large-scale collapse, acting as a piston that compresses the underlying air. Therefore, the roof collapse is modeled as a free-fall motion driven by its self-weight and the gas pressure in the goaf;

(3) Considering the short duration of the impact airflow disaster and the influence of gas viscosity, it is assumed that the air in the goaf has no time to flow back into the upper space and fully participates in the disaster process. This worst-case assumption yields the maximum possible influx of hazardous gases, providing a basis for ventilation safety redundancy design;

(4) The roadways connected to the 30110 working face are several kilometers long, so the shock airflow cannot reach the boundary within seconds. To obtain a closed-form solution, the roadway length $L_3$ is taken as infinite, which corresponds to a closed boundary at infinity; as this exerts negligible influence on the far-field wind speed, it is effectively equivalent to an unclosed boundary.

The gravity of the roof collapse is as follows:

$$W = \rho_d g L_1 L_2 h_1 \tag{1}$$

where $\rho_d$ is the density of the roof of the upper coal seam, kg/m$^3$; $g$ is the gravitational acceleration, N/kg; $L_1$, $L_2$, and $h_1$ are, respectively, the length, width, and thickness of the roof collapse block in the goaf, m.

The gas pressure acting on the collapse block (upward) is as follows:

$$F_1 = L_1 L_2 P_z \tag{2}$$

where $P_z$ is the air pressure in the goaf when the impact airflow disaster occurs, Pa, which is a function of the roof drop height $z$ or volume $V$.

The vertical coordinate system is established, and the block falling process is $z \in [0, M]$, so the motion equation of the block falling is $W - F_1 = m\alpha$. Thus, the acceleration of the falling block can be obtained as follows:

$$\alpha = g - \frac{P_z}{\rho_d h_1} \tag{3}$$

where $m$ is the mass of the roof collapse block, kg.

Since it is assumed that the change process of impact airflow is an isothermal process, from the starting position $z = 0$ of the roof block falling to any position $z$, it is as follows:

$$p_0 V_{z=0} = p_z V_z \tag{4}$$

At the moment when the roof block just begins to fall, the goaf volume is $V_{z=0} = V_0 + ML_1L_2$; When the descent distance is $z$, the volume of the goaf is $V_z = V_0 + (M-z)L_1L_2$. Substituting $V_0$ and $V_z$ into Equation (4), $p_z$ can be solved as follows:

$$p_z = \frac{V_0 - V_E + ML_1L_2}{V_0 - V_E + (M-z)L_1L_2} p_0 \tag{5}$$

where $V_0$ is the volume at the end of the impact airflow, mainly comprising the volume of the upper goaf, $m^3$; $M$ is the mining height of the upper coal seam, that is, the vertical falling distance of the roof block, m; $p_0$ is the gas pressure in the upper goaf of the working face before the disaster, Pa. $V_E$ is the discharge volume of impact airflow under initial pressure, $m^3$.

Based on the relationship between acceleration and velocity, substituting $\alpha = \frac{dv_z}{dt}$ into Equation (5) and subsequently substituting Equation (3) into $\alpha = \frac{dv_z}{dt}$ yields the following expression:

$$\frac{dv_z}{dt} = g - \frac{V_0 - V_E + ML_1L_2}{\rho_d h_1 [V_0 - V_E + (M-z)L_1L_2]} p_0 \tag{6}$$

Equation (6) represents the mathematical model (controlling equation) for impact flow disasters involving air from the goaf during the descent of the roof block. The model indicates that the roof block descent constitutes a variable-acceleration motion influenced by gas pressure.

The descent velocity $v_z$ of the roof block is determined not only by the height and area of the goaf and the air pressure but also by the block's mass and total descent height. Equation (6) allows the calculation of velocity $v_z$ at different times during the roof collapse.

When the roof block descends, the exit opening is much smaller than the goaf area. As a result, the airflow velocity within the goaf increases sharply, accompanied by the compression of air. For simplification, the exit cross-sectional area of the impact airflow is idealized as $A_1$. By applying the mass conservation (continuity) equation for an inviscid compressible fluid, the relationship between the cross-sectional area of the goaf 1 and the exit cross-sectional area 2 is expressed as: $\rho_1 A_0 v_z = \rho_2 A_1 v_2$. Accordingly, the average wind speed within the goaf can be obtained as:

$$v_2 = \frac{\rho_1 L_1 L_2 v_z}{\rho_2 A_1} \tag{7}$$

In this equation, $\rho_1$ and $\rho_2$ represent the air densities at the upper goaf of the working face and at the ideal exit of the impact airflow, respectively, $kg/m^3$. $A_1$ denotes the ideal

outlet area of the impact airflow, $m^2$, while $v_2$ indicates the airflow velocity at the ideal outlet cross-section, m/s.

$$A_1 = n_N A_N + n_L A_L + n_C A_C \tag{8}$$

where $n_N$, $n_L$, and $n_C$ denote the rock porosity in the natural deposition zone, load-affected zone, and compacted stable zone, respectively. Similarly, $A_N$, $A_L$, and $A_C$ represent the areas of these zones, respectively, $m^2$.

According to Equation (7), the velocity of the impact airflow during a large-scale roof collapse can be uniquely determined. In contrast, solving for $v_z$ in Equation (6) and subsequently determining $v_2$ is highly challenging. This difficulty arises because $v_z$ is a function of time ($t$) and the subsidence position ($z$) of the roof block. Moreover, $z$ is a functional, expressed as $z = f(v_z, \alpha_z, t)$, where it depends on the subsidence velocity $v_z$, acceleration $\alpha_z$, and time $t$. Therefore, a numerical differential method must be employed.

Within the micro-time interval $\Delta t \in [t_n, t_{n-1}]$, the velocity increment of the block is denoted as $\Delta v_z$. By replacing the differential in Equation (6) with the corresponding finite difference and introducing $\Delta v_z = v_{z,t_n} - v_{z,t_{n-1}}$, the resulting expression is as follows:

$$v_{z,t_n} = v_{z,t_{n-1}} + \left\{ g - \frac{V_0 - V_E + ML_1L_2}{\rho_d h_1 [V_0 - V_E + (M-z)L_1L_2]} p_0 \right\} \Delta t \tag{9}$$

Since Equation (8) involves the variable $z$, within the interval $\Delta t \in [t_n, t_{n-1}]$, it follows that $d_z/d_t = v_z$. Substituting the differential with a finite increment then yields $z_{t_n} = z_{t_{n-1}} + v_{z,t_{n-1}} \Delta t$.

Given the initial and boundary conditions $v|_{t=0,z=0} = 0$ and $z|_{t=0} = 0$, the block descent velocity at time $t_1$ is estimated using $v_{z_1,t_1} = g\Delta t$. This enables the computation of the remaining descent positions $z_{t_n}$ and $v_{z_{t_n},t_n}$ at other time instances using the aforementioned finite difference method. Subsequently, the time-dependent velocity of the impact airflow can be obtained from Equation (7):

$$v_{2,t_n} = \frac{\rho_1 L_1 L_2}{\rho_2 A_1} \left\{ v_{z,t_{n-1}} + \left\{ g - \frac{V_0 - V_E + ML_1L_2}{\rho_d h_1 [V_0 - V_E + (M-z)L_1L_2]} p_0 \right\} \Delta t \right\} \tag{10}$$

Based on the velocity of the impact airflow, the impact air discharge volume $V_E$ under the initial pressure can be obtained as follows:

$$V_{E,t_n} = \sum_{i=1}^{n} v_{2,t_{n-1}} A_1 \Delta t \tag{11}$$

The parameter values for the theoretical model of the impact airflow velocity are shown in Table 1.

**Table 1.** Parameters of the theoretical model of the speed of impact gas flow.

| Parameter | Value | Parameter | Value |
|---|---|---|---|
| $\rho_d$ (kg/m$^3$) | 2600 | $p_0$ (Pa) | $8.782 \times 10^4$ |
| $L_1$ (m) | 500 | $V_0$ (m$^3$) | $1.25 \times 10^5$ |
| $L_2$ (m) | 100 | $\rho_1$ (kg/m$^3$) | 1.2896 |
| $h_1$ (m) | 10 | $\rho_2$ (kg/m$^3$) | 1.29 |
| $M$ (m) | 2.5 | $A_1$ (m$^2$) | 6125 |

Figure 3 illustrates the temporal evolution of the impact airflow velocity and roof displacement. During the large-scale roof collapse in the goaf that triggered the impact airflow hazard, the process had transient and brief characteristics. The impact airflow velocity followed a pattern of initial increase followed by a decrease over time, which can

be divided into two phases: significant velocity increase and rapid velocity decrease. During the phase of significant velocity increase, the flow velocity instantaneously rises from zero, with the rate of increase gradually diminishing, reaching a maximum of 32.165 m/s at 0.832 s. In contrast, during the phase of rapid velocity decrease, the velocity rapidly declines from 32.165 m/s, reaching a minimum at 1.017 s. This latter phase represents the attenuation stage of the impact airflow. Throughout the entire process, the roof block displacement exhibited an exponential growth trend. The roof block collapsed and compressed the gas while simultaneously allowing leakage from the goaf. Once the roof block displacement reached the height of the goaf, the impact airflow was completely discharged, carrying harmful gases from the coal seam goaf into the working face.

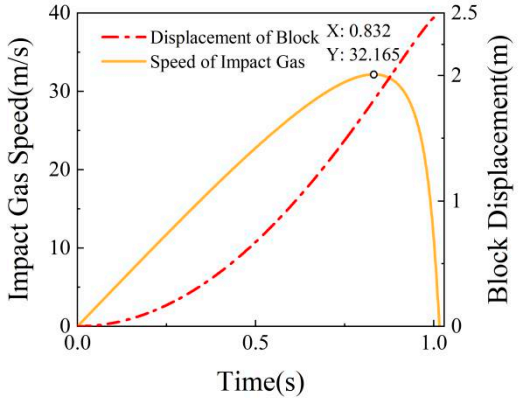


**Figure 3.** Impact gas speed and block displacement.

### *2.3. Variation Patterns of Factors Influencing Impact Airflow*

The collapse volume of the hard roof in the upper goaf, mining height, and density have significant effects on the evolution process of the impact airflow, as shown in Figure 3. With the increase in the collapse volume of the upper hard roof, the evolution duration of the impact airflow shortens. When the collapse volume increases from 450 × 90 × 9 $m^3$ to 550 × 110 × 11 $m^3$, the time for impact airflow to reach peak velocity decreases from 0.824 s to 0.802 s, while the peak velocity significantly increases from 27.117 m/s to 45.093 m/s, representing an increase of 66.29%, as shown in Figure 4a. The displacement of roof blocks also exhibits an increasing trend, indicating that the increase in collapse volume significantly enhances the intensity of impact airflow. As shown in Figure 4b, with the increase in mining height in the upper goaf, the evolution time of impact airflow extends. When the mining height increases from 2 m to 3 m, due to the increased roof collapse time, the time for impact airflow to reach peak velocity is correspondingly delayed, while the peak velocity increases from 31.8 m/s at 0.726 s to 38.867 m/s at 0.906 s, indicating greater kinetic energy, whereas the roof block displacement remains unchanged. Figure 4c demonstrates the influence of hard roof density on the evolution characteristics of impact airflow. With the increase in hard roof density in the upper goaf, the mass of the hard roof increases, the evolution duration of impact airflow shortens, and the time for impact airflow to reach peak velocity shows little change, but the peak velocity exhibits an upward trend. A larger collapse volume releases greater gravitational potential energy, which translates directly into the kinetic energy of the gas. Concurrently, the expanded collapse void mitigates flow resistance, leading to a substantial surge in peak airflow velocity. Our findings corroborate the work of Tu et al. [24], who identified the collapse scale as the dominant factor governing impact intensity in shallow coal seam hard roofs.

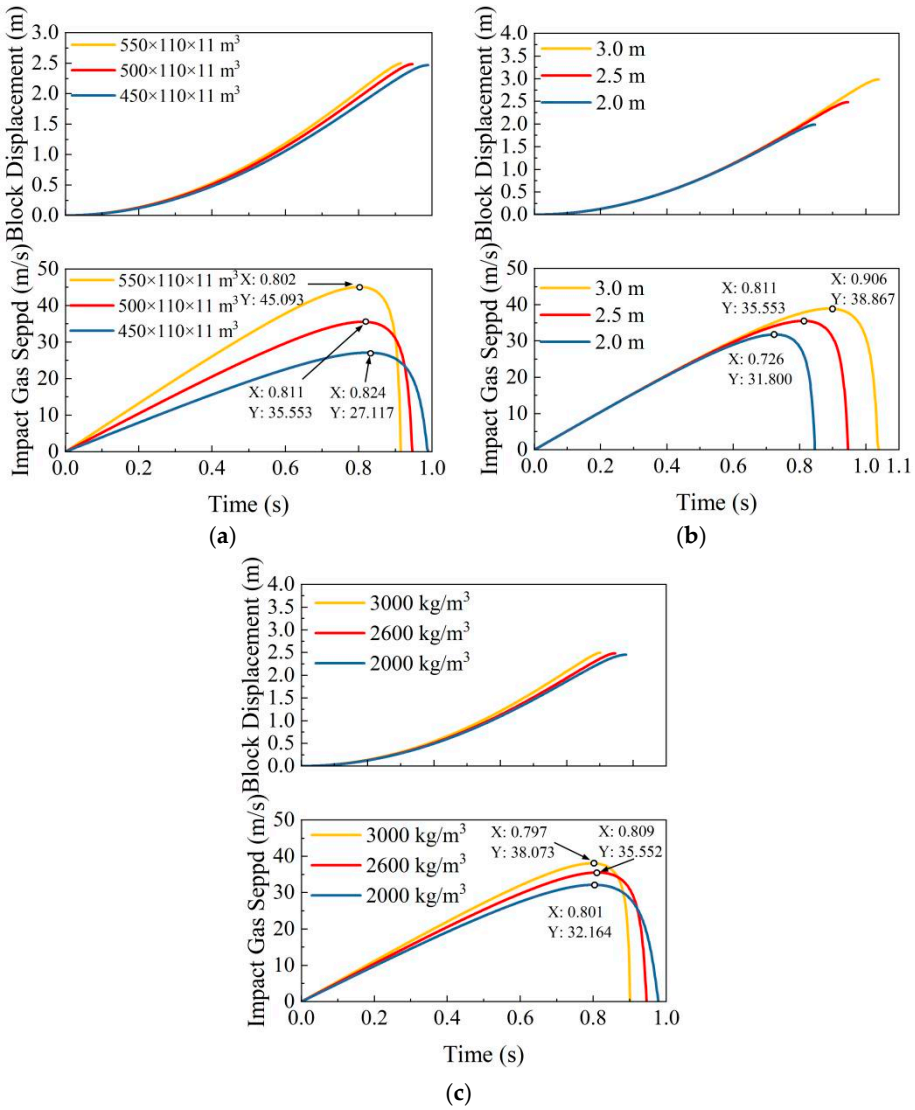


**Figure 4.** Influence factors of the impact gas flow. (**a**) Block size. (**b**) Height of upper goaf. (**c**) Hard roof density of upper goaf.

## 3. Engineering Condition

### *3.1. General Situation of the Fire Area in the 30110 Working Face*

The 30110 working face of the $3^{-1}$ seam has a mining height of 3.1 m, a dip length of 250 m, and a strike length of 1,979 m. The ventilation system employs a U-shaped configuration, as illustrated in Figure 5. Field investigations conducted through upper goaf boreholes revealed extensive fire zones near the upper section of the 30110 return gateroad. These fire areas exhibit irregular geometry with elongated distributions that are confined near the upper portion of the 30110 return gateroad and extend toward adjacent $3^{-1}$ seam working faces in the direction of both the main gateroad and the secondary main gateroad of the 30110 working face. During 30110 working face operations, frequent abnormal CO emissions occurred, significantly compromising working face safety and production efficiency.

### *3.2. Connectivity Analysis of Working Face and Upper Goaf*

As the working face advances, the overlying strata of the goaf gradually develop, forming a caved zone, a fractured zone, and a bending subsidence zone. Within the caved zone, most rock masses have already fallen into the goaf; strata in the fractured zone undergo significant downward-bending deformation with extensive fracture development, whereas strata in the

bending subsidence zone exhibit minimal downward-bending deformation and generally maintain good integrity. The fractured zone serves as a crucial pathway connecting the coal seam mining working face in close-distance coal seams to the overlying goaf. The porosity distribution of the fracture-filled rock mass in the goaf is shown in Figure 6.

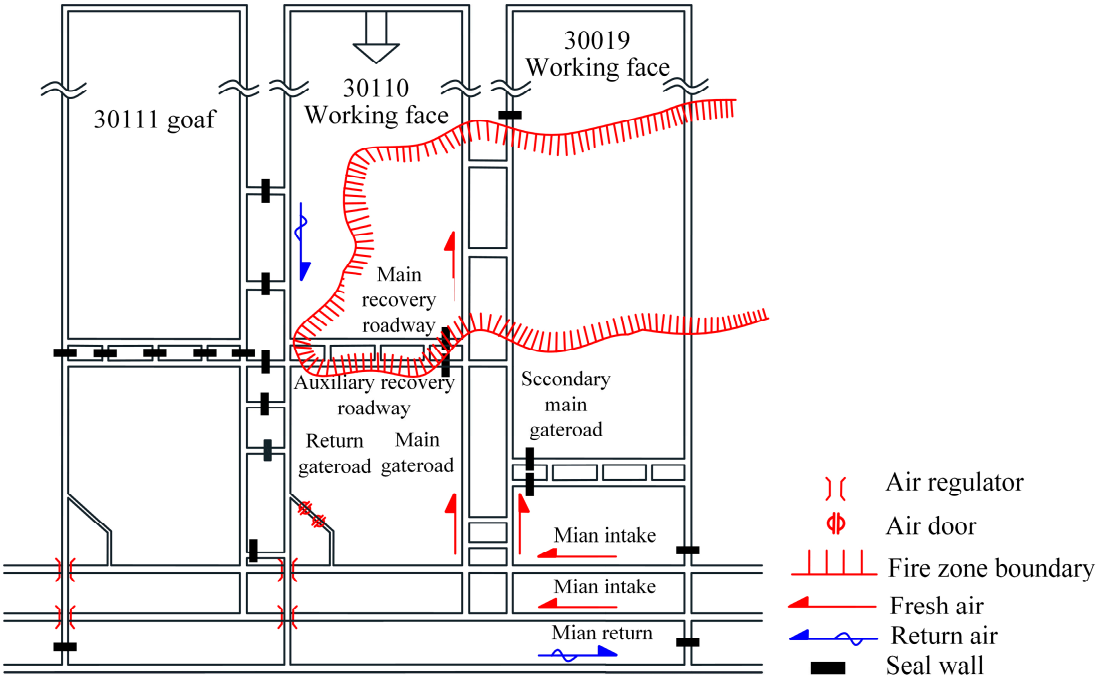


**Figure 5.** Layout of the 30110 working face and fire zones in the goaf of the $2^{-2}$ seam.

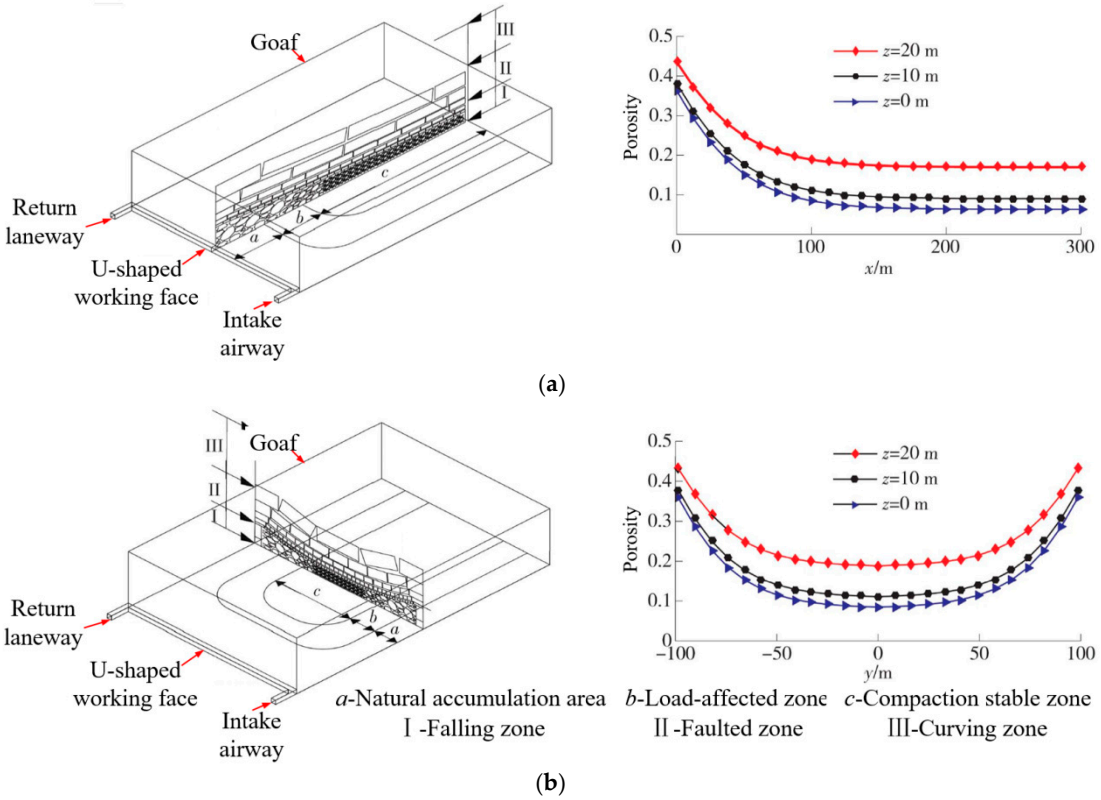


**Figure 6.** Porosity distribution of fractured rock mass. (**a**) Porosity distribution of fractured rock mass in the strike direction. (**b**) Porosity distribution of fractured rock mass in the dip direction.

A large amount of CO has been detected in the $2^{-2}$ seam goaf above the 30110 working face. As the principal pathway linking the $2^{-2}$ seam goaf to the 30110 working face, the development height of the fracture zone directly determines the effectiveness of CO seepage channels. Whether CO from the upper goaf can enter the working face through air leakage primarily depends on the relationship between the height $H_l$ of the fractured zone in the goaf behind the working face and the distance $H$ between the working face and the floor of the $2^{-2}$ seam goaf. When $H_l \geq H$, the fracture zone extends through both coal seams, creating a potential pathway for CO migration from the $2^{-2}$ seam goaf into the working face via air leakage. Conversely, when $H_l < H$, the risk of CO inrush into the working face through air leakage is significantly reduced.

The height of the caved zone depends on the mining height of the working face and the bulking factor of the rock, and its height $H_k$ can be estimated using the following empirical formula:

$$H_m = \frac{M}{(k-1)\cos\alpha} \tag{12}$$

where $M$ is the mining height, m; $k$ is the average bulking factor of caved rock; and $\alpha$ is the dip angle of the coal seam, °.

The bulking factor of rock mass depends on the rock properties; hard rock exhibits a larger bulking factor, while soft rock has a smaller bulking factor. The bulking factor is always greater than 1, generally ranging from 1.05 to 1.80.

According to the lithology distribution between the $2^{-2}$ and $3^{-1}$ seams, the lithology of the 30110 working face consists mainly of siltsto ne and fine-grained sandstone, and the average bulking factor $k$ of caved rocks is 1.5. The $3^{-1}$ seam is a near-horizontal coal seam with $\alpha = 0°$. Based on the actual conditions of the working face, the mining height $M$ = 3.1 m, and the calculated height of the caved zone $H_m$ = 6.2 m.

Generally, the empirical formula for the height of the fracture zone is as follows:

$$H_l = \frac{100\,M}{aM+b} \pm c \tag{13}$$

where $a$, $b$, and $c$ are constants to be determined, which can be determined according to the coal mine design code.

The immediate roof of the 30110 working face is mainly composed of siltstone and fine-grained sandstone, forming a relatively hard roof. Based on these lithological characteristics, the parameters are taken as $a$ = 1.6, $b$ = 3.6, and $c$ = 5.6, yielding a calculated fracture zone height of $H_l$ = 30.6∼41.8 m. Considering that the height of the collapse zone is 6.2 m, the overall fracture zone height ranges from 6.2 m to 30.6–41.8 m. According to the specific situation of the 30110 working face, which has been drilled into the goaf, the roof of the 30110 working face is approximately 37.6–44 m above the goaf of the $2^{-2}$ seam. Since the maximum fracture zone height exceeds the minimum coal-seam spacing, this indicates a potential overlap between the upper limit of the fracture zone and the lower boundary of the $2^{-2}$ seam goaf, thereby providing conditions for connectivity and the formation of air leakage channels. Consequently, CO accumulated in the $2^{-2}$ seam goaf may migrate into the 30110 working face through air leakage pathways.

## 4. Numerical Simulation of the Impact Airflow and the Abnormal Gush of Harmful Gas Induced by the Hard Roof Collapse

Currently, most coal mines employ the exhaust ventilation system. When subjected to roof collapse impacts from overlying goafs, the ventilation effectiveness and safety performance undergo significant changes. Accurate prediction and evaluation of system performance under the impact airflow are crucial for guiding practical engineering appli-

cations. Therefore, this study conducted numerical simulations of the exhaust ventilation system implementation at the 30110 working face. Using ANSYS Fluent 2022 R2 software, numerical simulations were performed to analyze impact airflow and abnormal harmful gas emissions induced by the hard roof collapse in the overlying goaf of the 30110 working face under the exhaust ventilation system. The study investigated the dynamic air leakage distribution characteristics within the $3^{-1}$ seam goaf and the infiltration and diffusion behavior of CO, aiming to provide reliable theoretical support for ventilation system engineering applications.

### 4.1. Physical Model Construction and Meshing

Fluent was employed to simulate the impact airflow and the abnormal emission of harmful gases induced by the hard roof collapse. The geometric parameters of the 30110 working face are provided in Table 2.

**Table 2.** Geometric parameters of the physical model.

| Position \ Geometric Size | Length/m | Width/m | Height/m |
|---|---|---|---|
| Working face | 250 | 5 | 3.1 |
| Upper goaf | 250 | 120 | 37.6 |
| Intake airway | 5 | 5.6 | 3 |
| Return airway | 5 | 5.3 | 3.2 |

ICEM CFD was used to establish the 3D model of the working face, with the coordinate origin located outside the return airway. The submap method was applied to partition irregular regions into several regular subregions, each discretized with structural grids. The entire model comprises approximately 250,000 cells, all of which are hexahedral. The schematic diagram of grid division is shown in Figure 7.

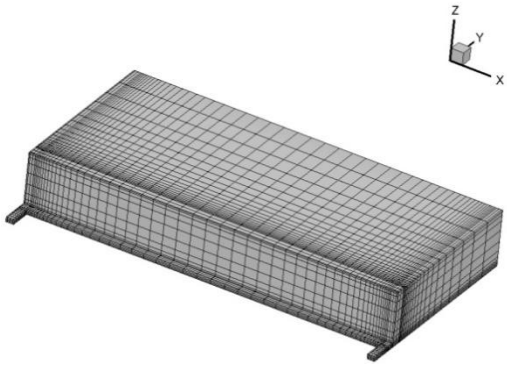


**Figure 7.** Mesh generation of 30110 goaf.

### 4.2. Boundary Conditions and Parameter Settings

The simulation was carried out using a pressure-based transient solver. The Standard k-ε turbulence model was adopted to simulate the flow field during the roof collapse process. The PISO algorithm was employed for pressure–velocity coupling. A second-order upwind scheme was applied to discretize the momentum, turbulent kinetic energy, and CO transport equations to ensure numerical accuracy. Owing to the presence of the goaf (modeled as a porous medium), the PRESTO scheme was chosen for pressure discretization, and the time step was set to 0.05 s. The convergence criterion for the energy equation was $10^{-6}$, while for all other equations it was $10^{-4}$. The goaf was represented as a porous zone with a porosity of 0.25; the viscous and inertial resistance coefficients were calculated

using the Ergun equation. A graphical flowchart illustrating the simulation procedure is provided in Figure 8. The boundary conditions and associated parameters, determined from on-site measurements, are summarized in Table 3.

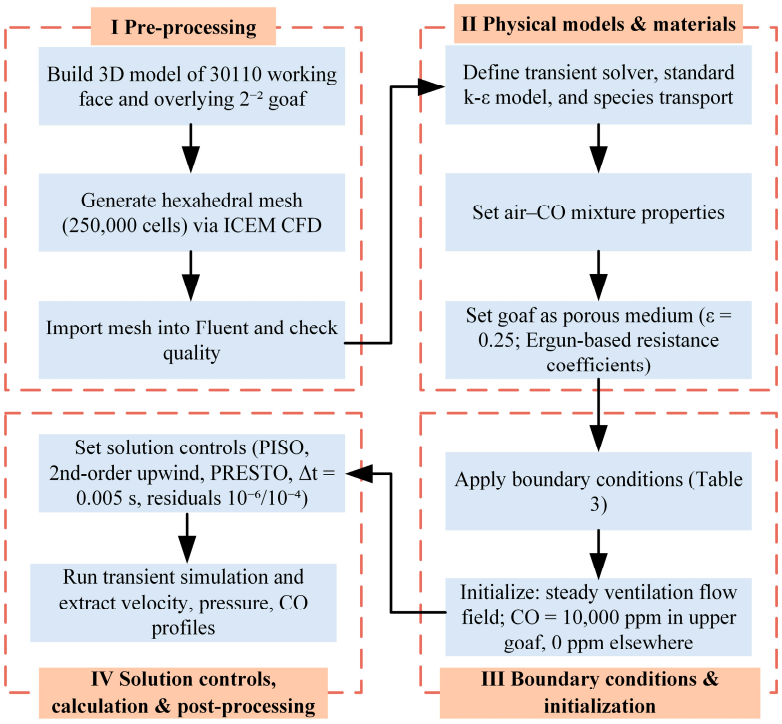


**Figure 8.** Graphical methodological workflow of the CFD simulation procedure.

**Table 3.** Boundary conditions and related parameters.

| Project | Parameter Setting |
|---|---|
| Intake airway pressure | 882.7 Hpa |
| Working face pressure | 882.7 Hpa |
| Return airway pressure | 882.6 Hpa |
| Upper goaf air pressure | 878.2 Hpa |
| CO concentration in the upper goaf | 10,000 ppm |
| The surface boundary of the intake airway and part of the upper goaf | VELOCITY_INLET |
| The boundary of the return airway | OUTFLOW |
| Goaf | Porous medium region |
| Viscous resistance coefficient | $1.35 \times 105\ m^{-2}$ |
| Inertial resistance coefficient | $840\ m^{-1}$ |

### 4.3. Analysis of Numerical Simulation Results

When the 30110 working face was under the exhaust ventilation, the air leakage velocity and distribution in the goaf of the upper $2^{-2}$ seam after a large-scale roof collapse occurred at 0.2, 0.4, and 1.1 s, respectively, as shown in Figures 9–11.

It can be observed from Figure 9 that when the roof of the $2^{-2}$ seam goaf collapsed at 0.2 s, the flow field state of the goaf changed abruptly, and the leakage flow velocity increased rapidly. At this time, the impact air velocity was in the stage of rapid increase, the compressed air surged toward the working face, and the gas in the goaf had entered the working face. The flow field at the return corner exhibited the largest change range, and the leakage velocity increased along the goaf toward the working face. The leakage velocity in the working face space increased from the intake corner to the return corner, with the return corner exhibiting the maximum velocity.

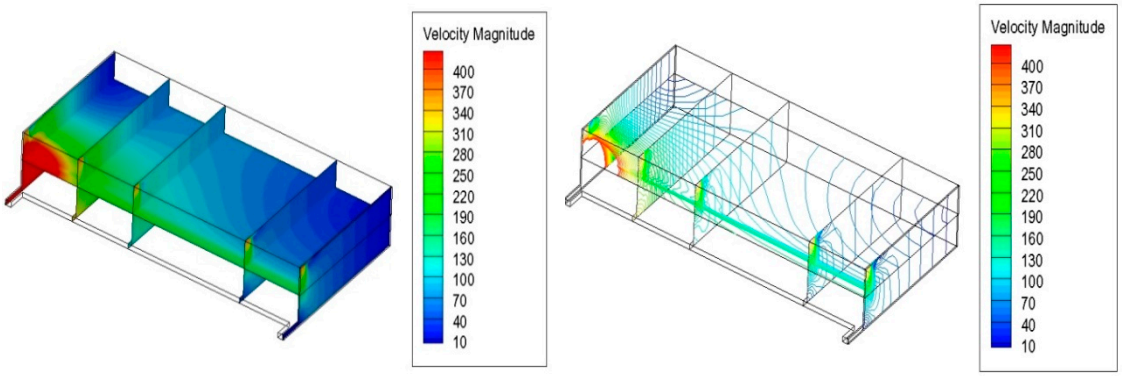


(**a**) (**b**)

**Figure 9.** Distribution of air leakage flow in the goaf (0.2 s after roof collapse). (**a**) Distribution diagram of air leakage velocity in the goaf (m/s). (**b**) Distribution diagram of air leakage wind speed profile in the goaf.

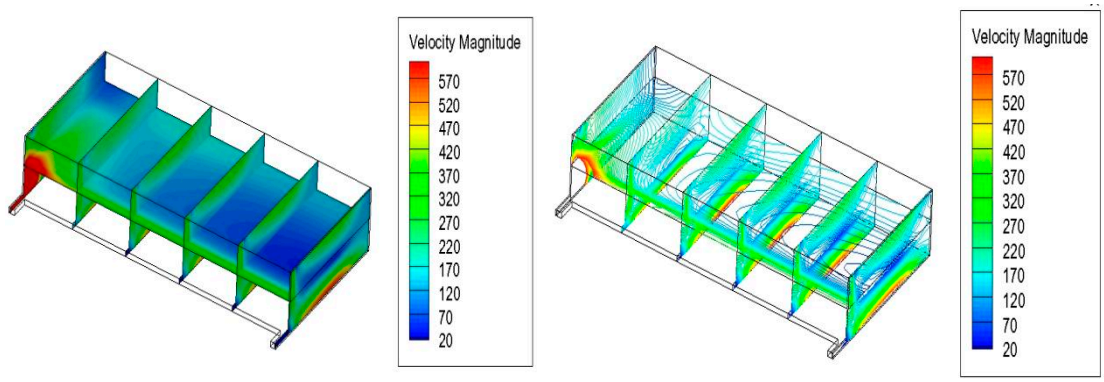


(**a**) (**b**)

**Figure 10.** Distribution of air leakage flow in the goaf (0.4 s after the roof collapse). (**a**) Distribution diagram of air leakage velocity in the goaf (m/s). (**b**) Distribution diagram of air leakage wind speed profile in the goaf.

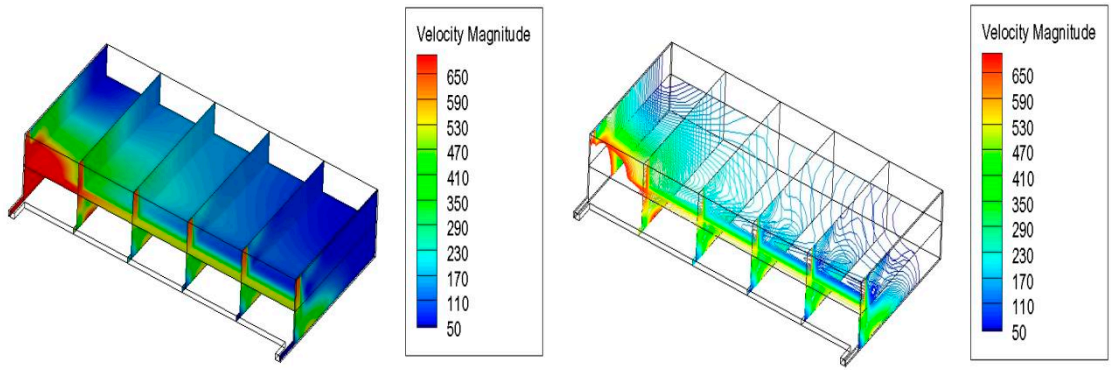


(**a**) (**b**)

**Figure 11.** Distribution of air leakage flow in the goaf (1.1 s after the roof collapse). (**a**) Distribution diagram of air leakage velocity in the goaf (m/s). (**b**) Distribution diagram of air leakage wind speed profile in the goaf.

When the roof of the $2^{-2}$ seam goaf collapsed at 0.4 s, as shown in Figure 10, the flow field of the goaf changed further, the impact air velocity was still in the stage of rapid increase, the leakage flow velocity increased rapidly, the air leakage flow velocity at the return corner was maximum, and the airflow velocity in the central area of the goaf behind the 30110 working face increased rapidly and gradually decreased toward both sides.

Figure 11 shows that when the roof of the $2^{-2}$ seam goaf collapsed at 1.1 s, although the flow field of the goaf was still in a state of change, the impact air velocity had entered the stage of rapid reduction, and the area at the return corner still maintained the maximum leakage flow velocity, but the rate of increase was significantly slower than that in the first 0.4 s, and the leakage flow velocity of the goaf behind the 30110 working face decreased. The high leakage flow rate region moved forward.

It can be concluded from Figures 9–11 that during the period of 0.2 to 1.1 s after the occurrence of large-area roof collapse in the goaf above the 30110 working face, the leakage flow velocity in the goaf increased rapidly and then slowed down. The change trend is consistent with the evolution of the impact airflow, which first intensified and then weakened. The simulated wind speed results align with the theoretical trends of impact flow analysis, thereby providing mutual verification of both the theoretical framework's accuracy and the numerical simulation's reliability. Throughout the entire process, the return corner was always the area with the maximum air leakage velocity, and the leakage velocity in the working face increased along the direction from the intake corner to the return corner. Under exhaust ventilation, a low-pressure zone forms on the return side, creating suction on the overlying goaf. This draws leakage air toward the return corner and accelerates the migration of hazardous gases from the upper goaf to the working face, making the return corner the primary pathway for abnormal gas outbursts [25].

When the 30110 working face operates under exhaust ventilation, the CO concentration and distribution in the $2^{-2}$ seam goaf are shown in Figures 12–14, respectively, when large-area roof collapse occurs at 0.2, 0.4, and 1.1 s.

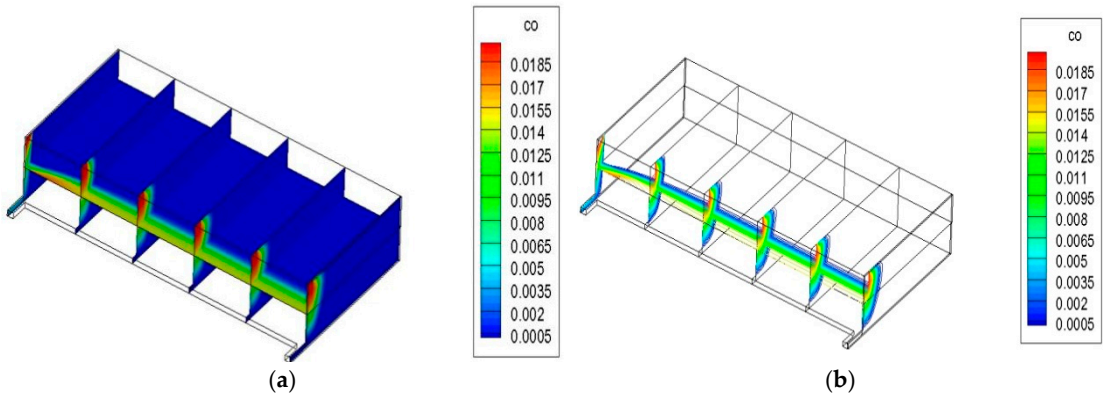


(**a**) (**b**)

**Figure 12.** Distribution of CO concentration in the goaf (0.2 s after roof collapse). (**a**) CO Concentration Distribution diagram ($^{0}/_{000}$). (**b**) Distribution diagram of the CO concentration profile.

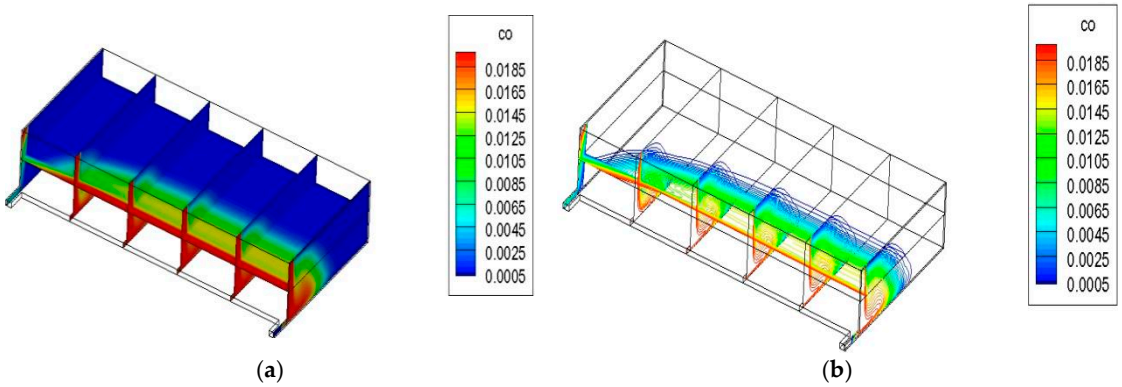


(**a**) (**b**)

**Figure 13.** Distribution of CO concentration in the goaf (0.4 s after roof collapse). (**a**) CO Concentration Distribution diagram ($^{0}/_{000}$). (**b**) Distribution diagram of the CO concentration profile.

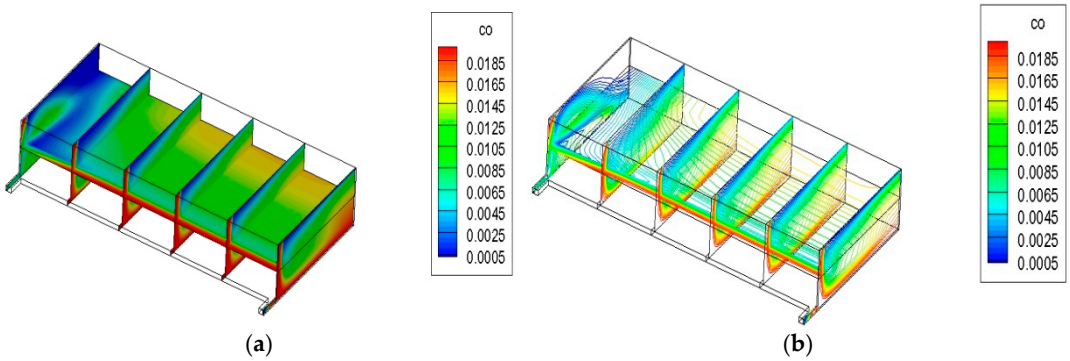


**Figure 14.** Distribution of CO concentration in the goaf (1.1 s after roof collapse). (**a**) CO Concentration Distribution diagram ($^{0}/_{000}$). (**b**) Distribution diagram of the CO concentration profile.

As shown in Figure 12, when the roof of the $2^{-2}$ seam goaf collapsed at 0.2 s, driven by the impact airflow, a large amount of CO in the goaf moved rapidly toward the working face and entered the working face through the goaf behind the working face, but the transport velocity was significantly lower than that of the impact airflow. At this time, the CO concentration at the return corner of the working face was the highest, reaching approximately 5000 ppm, which posed a serious threat to the safety of production at the working face, while the CO concentration in other areas of the working face was relatively low. When the roof collapses, the resulting shock airflow rapidly carries CO into the lower goaf. According to the velocity model, a larger collapse mass can drive the shock airflow above 45 m/s in less than 1 s, enabling it to penetrate the 37–44 m interburden almost instantaneously; as a result, the CO concentration at the return corner surges to 5000 ppm within 0.2 s. Overall, the CO concentration showed an increasing trend along the goaf toward the working face.

As shown in Figure 13, at 0.4 s, the CO concentration in the goaf near the working face increased sharply, and the CO accumulation range in the goaf behind the working face expanded rapidly. The return corner remained the area with the highest CO concentration in the working face. Meanwhile, the CO concentration in other areas of the working face also increased generally, and CO began to further diffuse from the intake and return air roadways in the working face.

When the roof of the $2^{-2}$ seam goaf collapsed at 1.1 s, as shown in Figure 14, the distribution range of high-concentration CO in the goaf behind the 30110 working face was further expanded, forming a large area of high-concentration CO distribution zone. The CO concentration in the working face continued to rise, and the CO concentration at the return corner remained at the highest level.

It can be concluded from Figures 12–14 that when exhaust ventilation is adopted at the working face, during the 0.2–1.1 s period following large-area roof collapse in the goaf above the working face, the high concentration of CO in the $2^{-2}$ seam goaf rapidly moves toward the 30110 working face, but the velocity is significantly lower than that of the impact airflow. As the area with the maximum air leakage velocity, the return corner of the working face becomes the primary pathway for CO entering the working face and the area with the highest concentration. With time progression, the CO concentration at the working face continues to rise, and the pollution range gradually expands to the intake and return airways of the working face, which seriously threatens the safety and production of the 30110 working face.

Under the current ventilation conditions at the 30110 working face, the exhaust ventilation system not only fails to effectively prevent abnormal harmful gas emissions from the overlying fire zones but also increases the risk of CO invasion due to its inherent suction

characteristics. Furthermore, the roof collapse duration and impact airflow evolution occur within extremely short timeframes, providing insufficient time for emergency evacuation and response by on-site personnel. Therefore, to effectively prevent and control the influx of abnormal and harmful gases during production operations, extend the time before impact airflow transports harmful gases into the working face, and provide critical response time for early warning systems and emergency rescue operations, this study proposes implementing a forced ventilation system as a technical solution.

## 5. A Forced Ventilation System

### 5.1. System Components

Based on the actual production layout of the 30110 working face and existing ventilation system conditions, a forced ventilation system comprising auxiliary fans, air doors, and air regulators was designed and constructed. The system configuration is as follows: two air doors were installed in the main gateroad upstream of the auxiliary recovery roadway; four sets of FBD №7.1/2 × 45 auxiliary fans were positioned in the main gateroad 1# Cut-through, with two units operating in parallel and two units serving as reserves; air regulators were installed in the return gateroad of the 30110 working face. The forced ventilation system utilizes auxiliary fans to supply air to the working face and employs air regulators in the return airway to control the pressure differential of the working face, thereby achieving pressure balance. The main performance parameters of the FBD №7.1/2 × 45 fans are presented in Table 4, while the specific location and system layout are illustrated in Figure 15.

**Table 4.** Main performance parameters of the fan.

| Type of Fan | Type of Motor | Speed (r/min) | Rated Voltage (V) | Flow Rate ($m^3$/min) | Pressure (Pa) |
|---|---|---|---|---|---|
| №7.1/2 × 45 | YBF2-225M-2 | 2960 | 660 | 730∼400 | 1100∼6000 |

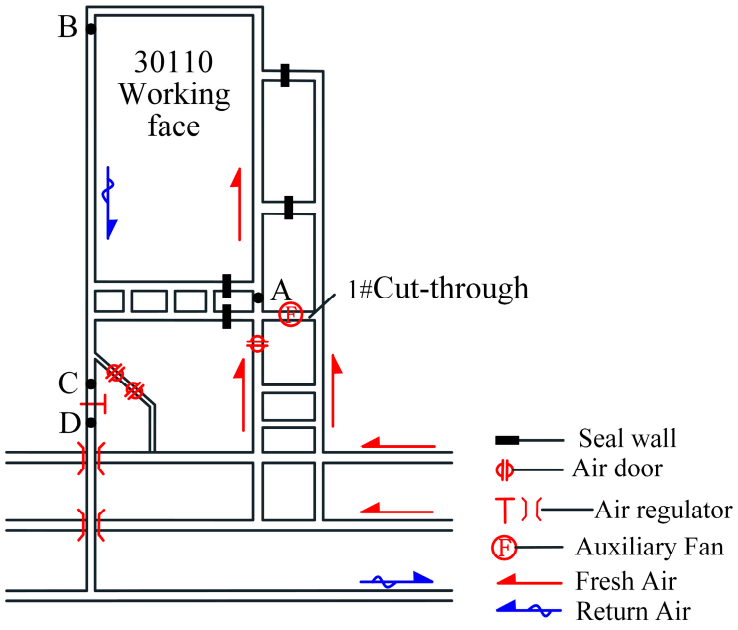


**Figure 15.** Pressure-balancing ventilation system of the 30110 working face.

It is important to note that there will be a significant change in pressure at both the working face and the upper fire area when the fan ceases operation and the roof collapses in the upper fire area. The regulation of pressure energy in the 30110 working

face ventilation system is accomplished through the air regulator. Manual adjustment is incapable of responding to dynamic air pressure changes in real time with sufficient accuracy. The automatic control system was constructed by combining the air regulators, the gas differential pressure sensors, the data acquisition system, and the actuator, which can realize the automatic control of the forced ventilation system. The determination of the safe operating range [$\Delta P_1$, $\Delta P_2$] for the inside and outside pressure differential of the air regulator was conducted based on actual working face conditions. When the actual pressure difference ($\Delta P$) received by the programmable logic controller (PLC) falls outside the safe range, the motor is immediately regulated through a frequency converter to adjust the effective ventilation area of the air regulator. This control process continues until $\Delta P$ is restored within the safe pressure range. The control system architecture and control process are illustrated in Figures 16 and 17.

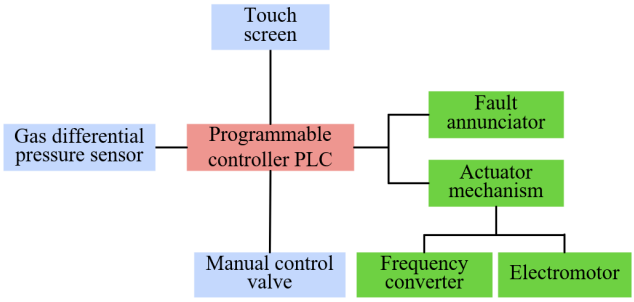


**Figure 16.** Automatic control system of pressure-balancing ventilation.

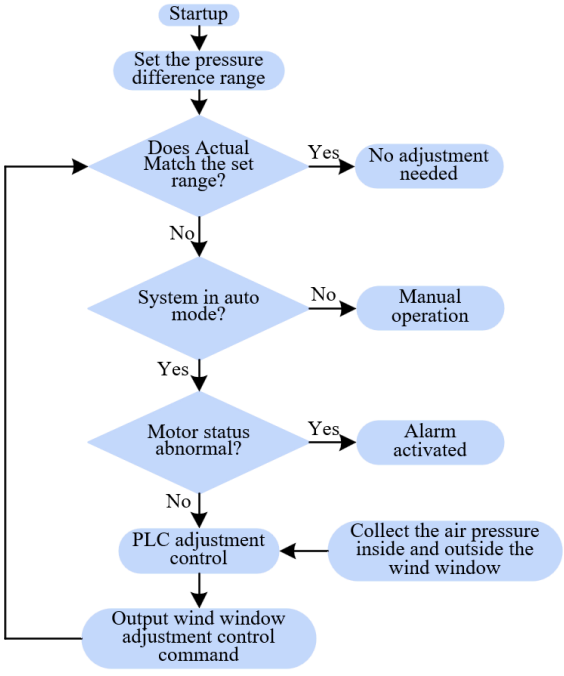


**Figure 17.** Control flow.

### *5.2. Regulation of the Forced Ventilation System*

A U-shaped water column (manometer) was installed in the main recovery gateroad of the 30110 working face and connected to the $2^{-2}$ coal seam goaf through a constructed borehole, enabling estimation of gas pressure in the overlying goaf based on gas pressure measurements in the main recovery gateroad and manometer readings, as illustrated in Figure 18. To ensure mining safety and stability, a 10% operational tolerance is incorporated. Accordingly, the pressure balance interface between the return corner and the $2^{-2}$ seam

goaf should be maintained within the range of 2$h$/5–3$h$/5. Following the implementation of the forced ventilation system in the 30110 working face, the air pressure within the working face exceeds that in the overlying goaf. To determine the pressure range required for stable operation of the exhaust ventilation system, the resulting gas pressure in the overlying goaf can be calculated using the following equation:

$$P_{goaf} = P' - P_U - \rho g h \tag{14}$$

where $P_{goaf}$ is the gas pressure of $2^{-2}$ seam goaf, Pa; $P'$ is the gas pressure in the main recovery gateroad, Pa; $P_U$ is the reading of the manometer, Pa; $\rho$ is the air density of the working face, kg/m$^3$; $g$ is the acceleration of gravity, N/kg; $h$ is the spacing between $2^{-2}$ and $3^{-1}$ seams, m.

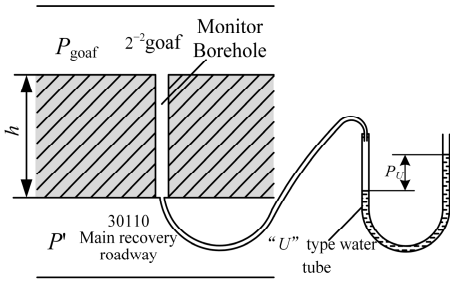


**Figure 18.** $2^{-2}$ Schematic diagram of goaf pressure calculation.

Four measurement points (A, B, C, and D) were established at the 30110 working face as shown in Figure 15, corresponding to locations upstream of the auxiliary fan, at the return corner, upstream of the air regulator, and downstream of the air regulator, respectively. Following the implementation of the forced ventilation system in the 30110 working face, air leakage from the face is not considered. The pressure energy loss $f_{AB}$ and $f_{BC}$ of the roadway in sections AB and BC are calculated by the following:

$$f_{AB} = (p_A - p_B) + (\frac{\rho_A}{2} {v_A}^2 - \frac{\rho_B}{2} {v_B}^2) + (\rho_A g z_A - \rho_B g z_B) = R_{AB} Q^2 \tag{15}$$

$$f_{BC} = (p_B - p_C) + (\frac{\rho_B}{2} {v_B}^2 - \frac{\rho_C}{2} {v_C}^2) + (\rho_B g z_B - \rho_C g z_C) = R_{BC} Q^2 \tag{16}$$

where $p_A$, $p_B$, and $p_C$ represent the gas pressure at points A, B, and C, respectively, Pa; $v_A$, $v_B$, and $v_C$ represent the wind speed at points A, B, and C, respectively, m/s; $v_A = Q/S_A$ and $v_B = Q/S_B$, $S_A$, $S_B$, and $S_C$ are the cross-sectional area of points A, B, and C, m$^2$; $\rho_A$, $\rho_B$, and $\rho_C$ represent the airflow density of points A, B, and C, respectively, kg/m$^3$; $z_A$, $z_B$, and $z_C$ represent the elevations of points A, B, and C, respectively, m; $R_{AB}$ and $R_{BC}$ represent the frictional resistance of the roadway in sections AB and BC, respectively, kg/m$^7$; and $Q$ represents the air volume of the working face, m$^3$/s.

The internal and external pressure difference ($\Delta P$) of the return gateroad can be calculated by the following:

$$\Delta P = P_C - P_D \tag{17}$$

If the pressure balance interface between the return corner of the working face and the overlying goaf is maintained within the range (2$h$/5, 3$h$/5), the gas pressure at the return corner must satisfy the following conditions:

$$P_{goaf} + \frac{7}{5}\rho g h < P_B < P_{goaf} + \frac{8}{5}\rho g h \tag{18}$$

Based on Equations (16)–(18), the pressure differential adjustment range ($\Delta P$) for the return air regulator can be determined as (338 Pa, 417 Pa).

### 5.3. Application Effect of the Forced Ventilation System

To evaluate the practical application effectiveness of the 30110 working face forced ventilation system and effectively control its operational state, this study systematically monitored the pressure differential between the 30110 working face and the $2^{-2}$ seam goaf, the pressure differential across the air regulator, and CO concentrations in the working face and return airflow.

Seven U-type manometers (designated 1# to 7#) were installed through boreholes in the 30110 working face. Manometers 1# through 6# were positioned at boreholes A6#, A8#, and A10# in the secondary main gateroad and at boreholes 3#, 4#, and 10# in the main recovery roadway to monitor the pressure differential between the 30110 working face and the $2^{-2}$ seam goaf. Manometer 7# was installed at the air regulator position in the return gateroad. Additionally, six CO sensors were positioned at the intake corner, return corner, return gateroad, and hydraulic supports 30#, 60#, and 90# for real-time monitoring of CO concentrations in the working face and return airflow. The specific locations of the U-type manometers and CO sensors are illustrated in Figure 19.

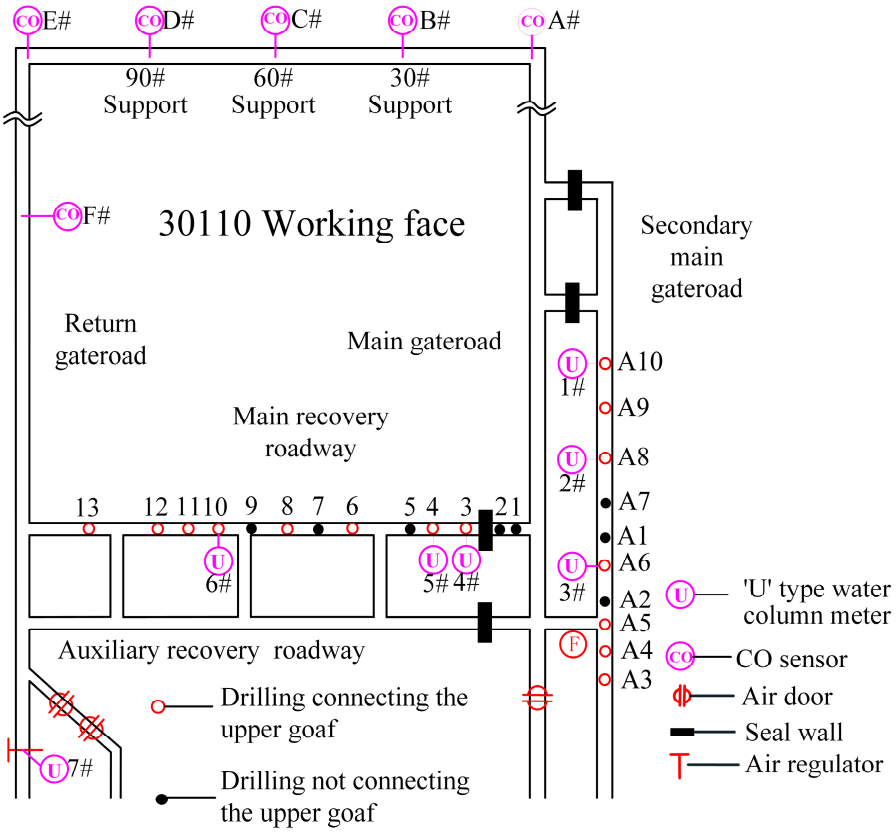


**Figure 19.** Layout of manometers and CO sensor.

As the working face advanced, CO concentrations exhibited an upward trend with distinct abnormal emission phenomena. When the working face advanced to approximately 40 m from the fire area boundary, CO concentrations reached a maximum of 37 ppm. The CO concentration monitoring results following implementation of the forced ventilation system in the 30110 working face are presented in Figure 20. The figure demonstrates that CO concentrations in the return corner—which exhibited the highest initial concentrations—decreased significantly from 36 ppm to 18 ppm within five days, representing a 50%

reduction. Concentrations subsequently continued to decline gradually and stabilized below 15 ppm, which was less than the maximum CO concentration requirements specified in the coal mine safety regulations. Furthermore, CO concentration reductions showed an increasing trend from the return corner toward the intake corner, with overall concentration levels decreasing progressively across the working face. After 15 days, CO concentrations at the intake corner remained consistently stable at 3 ppm or lower, occasionally reaching 0 ppm. No abnormal influx of CO occurred during the operation of the forced ventilation system. These results demonstrate that the forced ventilation system effectively reduces safety risks associated with hazardous gases, inhibits the harmful gas emissions, and significantly improves the overall safety conditions of the working face.

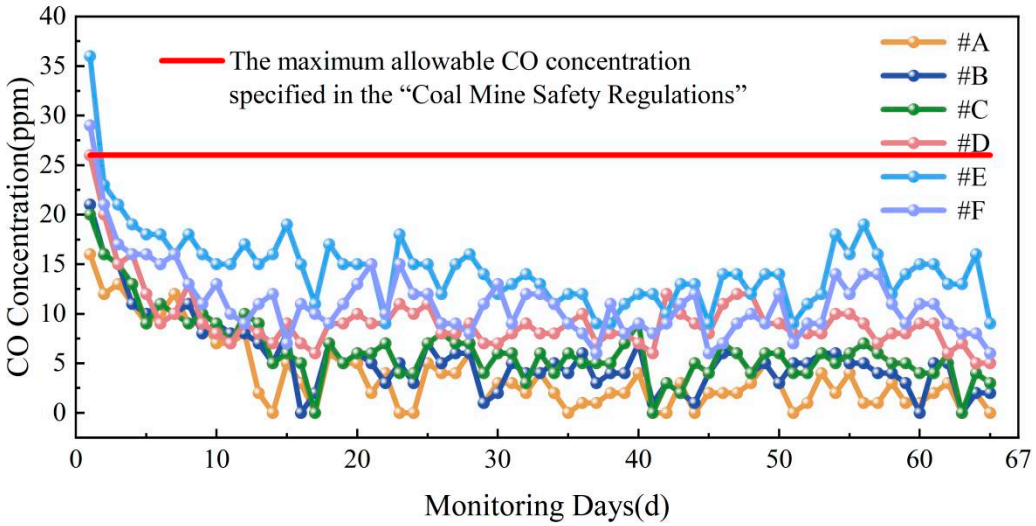


**Figure 20.** CO concentration change of the 30110 working face.

The pressure differential between the working face and the $2^{-2}$ seam goaf reflects the operational stability of the uniform-pressure ventilation system. As shown in Figure 21, during the differential pressure monitoring period, manometers 1# through 3# consistently fluctuated within the range of 110–120 Pa. Although readings occasionally fell below 100 Pa or exceeded 130 Pa during isolated times, they returned to the 110–120 Pa range shortly after appropriate adjustment of the air regulator. Manometers 4# through 6# fluctuated around 160 Pa during the initial 29 days. After the 29th day, the differential pressure values from these three manometers changed slightly but remained at relatively stable levels following system adjustments. These observations indicate that although the pressure differential between the working face and the $2^{-2}$ seam mined-out area exhibits some fluctuation, it remains generally stable, demonstrating stable operation of the forced ventilation system.

The pressure differential across the return air regulator should be maintained within the range of 338–417 Pa to ensure pressure balance and stability of the working face while preventing abnormal inrush of hazardous gases from the upper fire area into the working face and air leakage from the working face into the upper fire area. Manometer 7# readings serve as the direct basis for ventilation system adjustments. As shown in Figure 22, the readings from manometer 7# are consistently maintained between 340 and 360 Pa, remaining within the safe operating range of 338–417 Pa, which further confirms the good stability of the ventilation system.

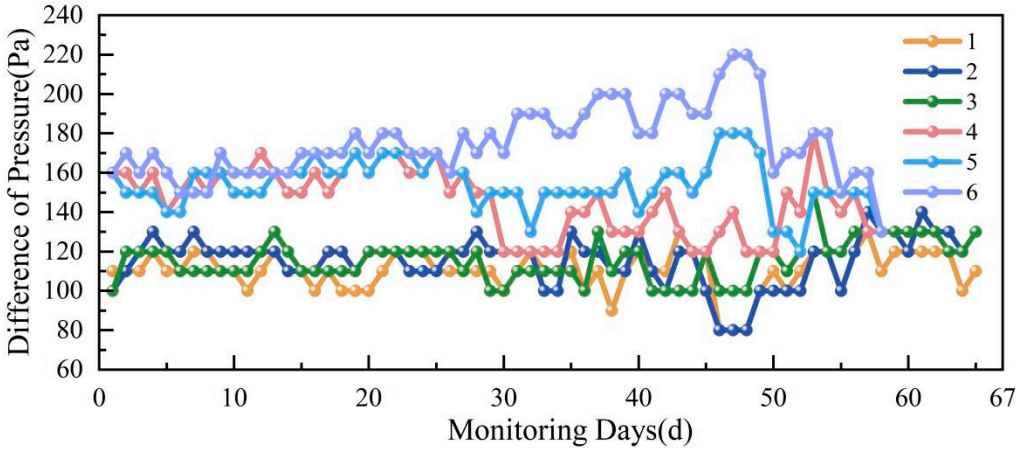


**Figure 21.** Pressure difference change of 1∼6# manometers.

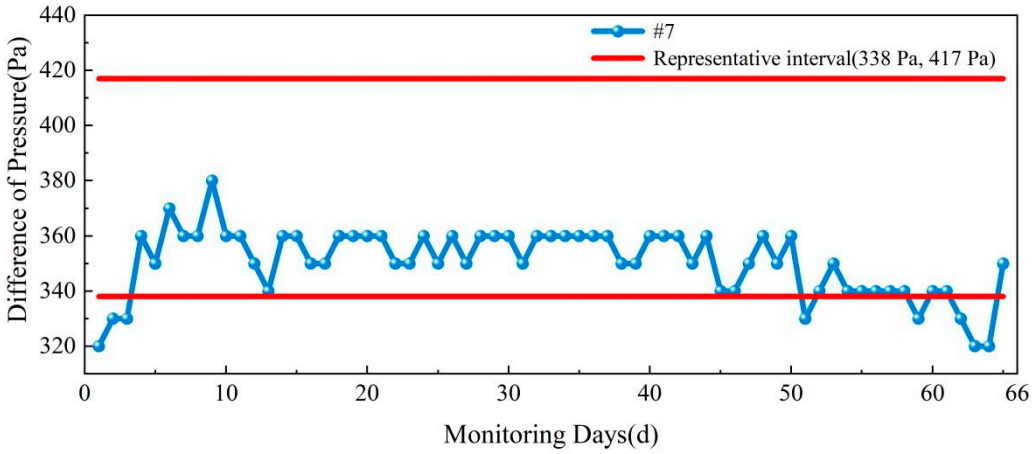


**Figure 22.** Pressure difference change of 7# manometer.

## 6. Automatic Control and Warning Technology of the Forced Ventilation System

Due to the sudden onset, short duration, and extensive impact range of large-scale roof collapses, their occurrence is often not immediately apparent. To maximize the active protection benefits of the forced ventilation system, early warning and timely treatment of abnormal influxes of harmful gases are carried out so as to effectively protect the personnel and ensure safe production on the working face. Therefore, it is essential to make full use of the mine safety monitoring system in conjunction with hazardous gas monitoring, pressure dynamic monitoring, and disaster early warning technologies. Accordingly, the monitoring and warning system of the ventilation system was constructed in the working face to realize the real-time dynamic monitoring and warning of the abnormal emission of harmful gases.

### *6.1. Pressure Mutation Monitoring and Alarm System*

Due to the occurrence of large area collapse in the upper goaf, the pressure mutation is bound to be ahead of the gas migration. By setting up a pressure mutation monitoring and alarm system in the working face, the pressure mutation in the upper goaf can be monitored in real time. Once the value reaches or exceeds the warning threshold, an alarm will be given immediately to prompt the operators in the working face to evacuate urgently. Thus, it can effectively prevent the abnormal influx of harmful gases from harming the workers and ensure life safety.

The system includes pressure sensors, data acquisition instruments, and sound and light alarms. The pressure sensor can monitor the pressure change in real time and transmit the pressure change data to the data acquisition instrument. When the pressure change reaches or exceeds the warning value, the data acquisition instrument will transmit the signal to the sound and light alarm, and the alarm will activate. A DYP gas pressure transmitter was used as the air pressure sensor. The data acquisition instrument adopts a four-channel digital display instrument with a full division number, which has strong anti-electromagnetic interference ability and can work stably in a strong electromagnetic interference environment. The full division number input can realize four different sensor signal inputs. Six pressure sensors were installed in the boreholes 3#, 4#, and 10# of the main recovery roadway and boreholes A6#, A8#, and A10# in the secondary main gateroad for the 30110 working face. Two data acquisition units are installed between boreholes #4 and #10 in the main recovery roadway and at the junction of the secondary main gateroad with the auxiliary recovery roadway. The power supply and relays for the alarms are located in the secondary main gateroad. As shown in Figure 23, three alarms are deployed at the following positions: the fan installation point in the auxiliary recovery roadway, the main gateroad, and the secondary main gateroad near the working face. The structural composition and schematic of the system are shown in Figure 24. Instrument parameters are shown in Table 5.

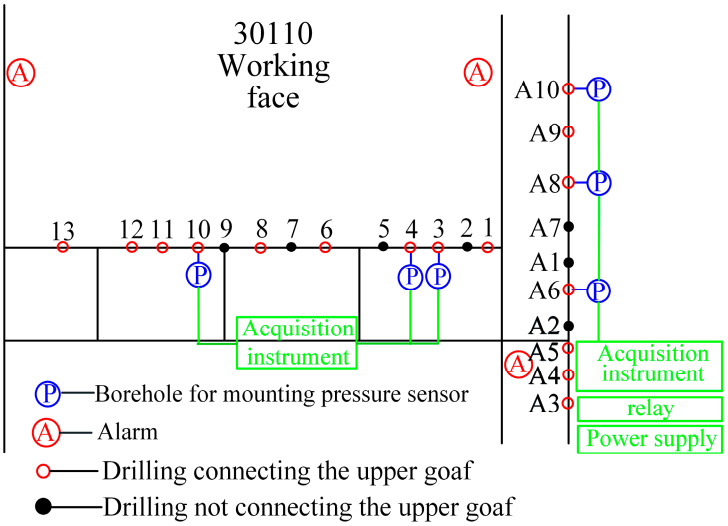


**Figure 23.** Layout of the pressure sensor in the 30110 working face.

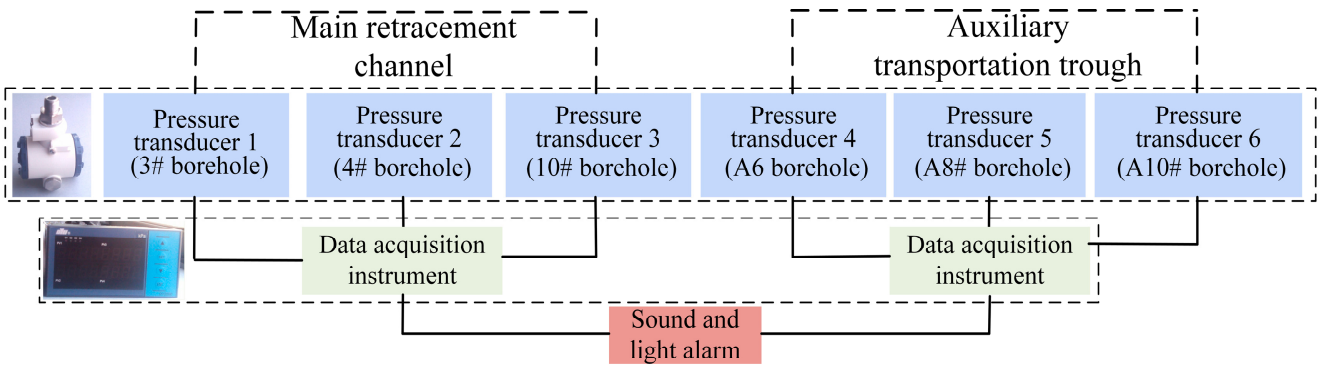


**Figure 24.** Structure composition and schematic diagram.

**Table 5.** Performance parameters of the instruments.

| Instrument | Accuracy | Operating Range | Acquisition Frequency |
|---|---|---|---|
| CO sensor | ±(100 + 3% of true value) ppm | 0–100,000 ppm | 50 Hz |
| DYP gas pressure transmitter | ±0.25% FS | 0–150 kPa | 50 Hz |
| Data acquisition instrument | ±0.5%FS | 4–20 mA/1–5 V | 50 Hz |

### *6.2. Monitoring and Warning System of Harmful Gas in the Working Face*

To monitor the abnormal changes in harmful gas in the working face in a timely and accurate manner and to realize danger warnings, the harm caused by abnormal influxes of harmful gas to workers is minimized. Six CO sensors were installed at the intake and return corners of the 30110 working face, at the return gateway, and at supports 30#, 60#, and 90#. The monitoring results were transmitted to the scheduling room in real time through the mine-monitoring system. Each sensor was connected to three alarm devices, installed in the working face, the main, and the return gateroad. When the CO concentration exceeded the set threshold, the sound and light alarms activated immediately, prompting underground operators to evacuate the working face. Additionally, a goaf beam pipe monitoring system was arranged in the working face, with one pipeline installed in the main gateroad and the return gateroad, covered with steel pipes for protection. As the working face advances, the beam tube is buried in the goaf. Gas samples from the gob behind the working face are collected daily in three shifts using the beam tube and analyzed with a gas chromatography analyzer to monitor CO concentration changes, enable early warning of abnormal CO influx, and allow timely measures to be taken. In addition, all personnel entering the working face must be equipped with functional portable gas detectors before entering the mine. This enables real-time monitoring of hazardous gas concentrations at the working face, serving as an effective complement to the monitoring system.

## 7. Security Technology of the Forced Ventilation System

### *7.1. Daily Production and Maintenance Management*

Firstly, the face operation personnel were streamlined and reasonably allocated. A daily maintenance period of four hours was established to perform overhauls on key equipment, including hydraulic supports and ventilation facilities. This scheduled maintenance helps prevent disturbances to the ventilation system and avoids abnormal influxes of CO caused by large-scale roof collapses ahead of the support frames. Additionally, the operation of the forced ventilation system is verified daily through checks of working face air volume, air pressure, and hazardous gas concentrations. All personnel are required to carry a self-rescue device at all times. Furthermore, five additional compressed oxygen self-rescue devices are stored for emergency use in both the main gateroad and the advanced support zone of the return gateroad. During working face retreat, to prevent operational vehicles from damaging ventilation facilities, equipment must be withdrawn sequentially from the tail to the nose in turn. Personnel and vehicles are required to operate exclusively on the fresh airflow side. Under abnormal conditions, the designated disaster avoidance route for the working face is as follows: return gateroad → working face → main gateroad → auxiliary adit → shaft head.

### *7.2. Special Security*

In response to emergencies such as the failure of the auxiliary fan, all power sources on the working face should be cut off immediately, including the shearer and conveyor. All operators in the working face should be led to evacuate to the auxiliary adit along the main

gateroad, and warning barriers should be set up at the entrance of the 30110 main gateroad and the air door around the 30110 return gateroad. Before restarting the equalizer fan, the gas concentrations within 10 m of the fan and its switch must be inspected. The fan may be restarted only when the gas and CO concentrations are below 0.5% and 24 ppm, respectively. After the auxiliary fan has been in operation for 30 min, and only after confirming that the air volume, airflow direction, air pressure, and gas concentrations have returned to and stabilized within normal ranges, personnel may be permitted to re-enter the working face.

## 8. Discussion and Outlook

(1) Based on basic assumptions, this study established a theoretical model for the impact airflow velocity induced by overlying roof collapse. Future work could incorporate the effects of goaf characteristics, roof lithology, and different collapse patterns on airflow initiation and migration.

(2) While this study offers a practical framework for suppressing impact airflow, two directions merit further work. First, the thermodynamic simplifications can be addressed by developing a multi-field coupling model that incorporates heat transfer from the goaf fire area so that the effect of thermal buoyancy on gas migration is captured. Second, numerical uncertainties can be reduced by integrating DEM with CFD to more realistically represent the irregular, discrete caving of hard roofs.

(3) This study determined the safe pressure-difference range for the air regulator in the exhaust ventilation system, enabling stable operation. However, this range is site-specific, derived from the interburden spacing and goaf compaction at this mine, and must be re-evaluated for other conditions. Moreover, fluctuations in the U-tube manometer readings indicated that the face-to-goaf pressure difference is influenced by strata pressure and barometric changes. The system currently depends on real-time monitoring; future work could introduce automatic control based on dynamic pressure changes in the upper goaf and working face, as well as abnormal gas influx, to enhance reliability and stability under complex conditions.

## 9. Conclusions

In this study, the harmful gas intrusion disaster in the overlying $2^{-2}$ seam goaf above the $3^{-1}$ seam at Longhua Coal Mine, Shaanxi Province, was taken as the research object. Based on a systematic analysis of the formation mechanism of the impact airflow, a theoretical velocity model of the impact airflow induced by roof collapse was established, and the key influencing factors and energy evolution characteristics were identified. Numerical simulations were then conducted to examine the spatial distribution of the impact airflow and associated CO emissions under exhaust ventilation. To effectively prevent abnormal CO influx from the overlying goaf, a forced ventilation system was designed and implemented at the working face, accompanied by monitoring, early-warning, and safety assurance technologies. This system has demonstrated significant effectiveness in enhancing the disaster resistance of the working face under extreme conditions of large-scale hard roof collapse. The research results indicate the following:

(1) The impact airflow velocity first increases sharply and then decreases rapidly. The roof block displacement grows exponentially. As the collapsed volume of the upper goaf increased from $450 \times 90 \times 9$ m$^3$ to $550 \times 110 \times 11$ m$^3$, the peak velocity rose from 27.1 to 45.1 m/s (a 66.3% increase). When the mining height increased from 2 m to 3 m, the peak velocity rose from 31.8 to 38.9 m/s. Increasing the density of the hard roof also drove the peak velocity higher.

(2) Under the exhaust ventilation, the goaf leakage velocity rises rapidly, with the return corner exhibiting the largest leakage flow and becoming the main pathway for CO

migration to the working face. This location also shows the highest CO concentration, reaching 5000 ppm at 0.2 s. The CO concentration at the working face continues to rise over time and diffuses into the working face, as well as the intake and return gateroads. The exhaust ventilation not only fails to suppress gas emissions from the overlying goaf but also intensifies the risk of CO invasion, leaving insufficient warning and response time, which leads to recurrent abnormal CO influx events.

(3) The forced ventilation system consists of two air doors, four auxiliary fans, and one air regulator. The pressure difference adjustment interval of the air regulator is (338 Pa, 417 Pa). Its application effectively suppressed CO migration from the upper goaf, reducing CO concentration at the return corner from 36 ppm to below 15 ppm. Meanwhile, the goaf pressure difference remained stable, the differential pressure across the air regulator stayed within a safe range, and the system maintained stable operation, thereby ensuring safe production at the working face.

(4) By integrating the mine safety monitoring system with dynamic air pressure monitoring, disaster early-warning technology, and harmful gas monitoring, a monitoring and early-warning system for the forced ventilation system was established at the working face. Through real-time monitoring of abrupt changes in pressure and CO concentration in the overlying goaf, the system enables timely detection and early warning of abnormal gas emissions. This not only supports the reliable operation of the ventilation system but also provides advanced warnings and critical evacuation time for personnel under extreme roof-collapse conditions.

**Author Contributions:** H.W.: Funding acquisition, Visualization, Supervision, Writing—review and editing, Investigation. C.Z.: Data curation, Writing—original draft, Funding acquisition, Visualization, Methodology, Conceptualization. F.Y.: Funding acquisition, Supervision, Data curation. Y.Z.: Funding acquisition, Validation, Resources, Investigation. Y.Y.: Methodology, Investigation, Validation. All authors have read and agreed to the published version of the manuscript.

**Funding:** This research is financially supported by the National Natural Science Foundation of China (51804058), the Sichuan Provincial Transportation Technology Project (2024-A-01), and the Sichuan Science and Technology Program (2025ZNSFSC0408).

**Data Availability Statement:** The original contributions presented in this study are included in the article. Further inquiries can be directed to the corresponding authors.

**Conflicts of Interest:** Authors Haiyang Wang, Feng Yang were employed by the Sichuan Highway Planning, Survey, Design and Research Institute Ltd. The remaining authors declare that the research was conducted in the absence of any commercial or financial relationships that could be construed as a potential conflict of interest.

## References

1. He, X.; Zhao, Y.; Yang, K.; Zhang, C.; Han, P. Development and formation of ground fissures induced by an ultra large mining height longwall panel in shendong mining area. *Bull. Eng. Geol. Environ.* **2021**, *80*, 7879–7898. [CrossRef]
2. Wang, T.; Wang, Q.; Shao, L.; Xia, Y.; Fu, X.; Ning, S.; Xie, Z.; Jiang, T. Current status of the research on coal geology in China. *Acta Geol. Sin.-Engl. Ed.* **2016**, *90*, 1284–1297. [CrossRef]
3. Ghasemi, E.; Shahriar, K. A new coal pillars design method in order to enhance safety of the retreat mining in room and pillar mines. *Saf. Sci.* **2012**, *50*, 579–585. [CrossRef]
4. Kobylkin, S.S.; Kharisov, A.R. Design features of coal mines ventilation using a room-and-pillar development system. *J. Min. Inst.* **2020**, *245*, 531–538. [CrossRef]
5. Du, E.; Zhou, X.; Zhou, N. Numerical simulation study on the failure characteristics of the combined structure of residual coal pillar and roof in room and pillar mining method. *Eng. Fail. Anal.* **2025**, *174*, 109531. [CrossRef]
6. Guo, L.; Tao, Z.; He, M.; Coli, M. Impact of Micro-NPR bolt on the mining of deep-buried phosphate via the room-and-pillar method. *Tunn. Undergr. Space Technol.* **2023**, *140*, 105326. [CrossRef]

7. Qiao, M.; Ren, T.; Roberts, J.; Yang, X.; Li, Z.; Wu, J. New insight into proactive goaf inertisation for spontaneous combustion management and control. *Process Saf. Environ. Prot.* **2022**, *161*, 739–757. [CrossRef]
8. Yi, X.; Zhang, M.; Deng, J.; Xiao, Y.; Chen, W.; Heris, S.Z. Effects on environmental conditions and limiting parameters for spontaneous combustion of residual coal in underground goaf. *Process Saf. Environ. Prot.* **2024**, *187*, 1378–1389. [CrossRef]
9. Kang, H.; Lou, J.; Gao, F.; Yang, J.; Li, J. A physical and numerical investigation of sudden massive roof collapse during longwall coal retreat mining. *Int. J. Coal Geol.* **2018**, *188*, 25–36. [CrossRef]
10. Zhou, A.; Zhang, M.; Wang, K.; Elsworth, D.; Wang, J.; Fan, L. Airflow disturbance induced by coal mine outburst shock waves: A case study of a gas outburst disaster in China. *Int. J. Rock Mech. Min. Sci.* **2020**, *128*, 104262. [CrossRef]
11. Xu, C.; Yang, T.; Wang, K.; Fu, Q.; Ma, S. Gas extraction of coal seam roof fractured zone in China: A review. *Fuel* **2024**, *357*, 129930. [CrossRef]
12. Wang, W.; Cheng, Y.; Wang, H.; Liu, H.; Wang, L.; Li, W.; Jiang, J. Fracture failure analysis of hard–thick sandstone roof and its controlling effect on gas emission in underground ultra-thick coal extraction. *Eng. Fail. Anal.* **2015**, *54*, 150–162. [CrossRef]
13. Wang, K.; Zhang, X.; Wang, L.; Li, L.; Zhang, M.; Zhou, A. Experimental study on propagation law of shock wave and airflow induced by coal and gas outburst in mine ventilation network. *Process Saf. Environ. Prot.* **2021**, *151*, 299–310. [CrossRef]
14. Cheng, L.; Xu, J.; Peng, S.; Yang, H.; Jiao, F.; Zhou, B.; Yan, F. Dynamic behavior of outburst two-phase flow in a coal mine T-shaped roadway: The formation of impact airflow and its disaster-causing effect. *Int. J. Min. Sci. Technol.* **2023**, *33*, 1001–1017. [CrossRef]
15. Xu, J.; Cheng, L.; Peng, S. Formation and propagation law of coal and gas outburst impact airflow. *J. China Coal Soc.* **2022**, *47*, 333–347. [CrossRef]
16. Wang, K.; Zhou, A.; Zhang, J.; Zhang, P. Real-time numerical simulations and experimental research for the propagation characteristics of shock waves and gas flow during coal and gas outburst. *Saf. Sci.* **2012**, *50*, 835–841. [CrossRef]
17. Sun, H.; Cao, J.; Li, M.; Zhao, X.; Dai, L.; Sun, D.; Wang, B.; Zhai, B. Experimental research on the impactive dynamic effect of gas-pulverized coal of coal and gas outburst. *Energies* **2018**, *11*, 797. [CrossRef]
18. Jin, K.; Cheng, Y.; Ren, T.; Zhao, W.; Tu, Q.; Dong, J.; Wang, Z.; Hu, B. Experimental investigation on the formation and transport mechanism of outburst coal-gas flow: Implications for the role of gas desorption in the development stage of outburst. *Int. J. Coal Geol.* **2018**, *194*, 45–58. [CrossRef]
19. Zhou, A.; Wang, K.; Feng, T.; Wang, J.; Zhao, W. Effects of fast-desorbed gas on the propagation characteristics of outburst shock waves and gas flows in underground roadways. *Process Saf. Environ. Prot.* **2018**, *119*, 295–303. [CrossRef]
20. Cheng, L.; Wang, M.; Jing, G.; Zhang, J. Gas explosion overpressure and impact airflow velocity attenuation model. *Explos. Shock Waves* **2025**, *45*, 082101. [CrossRef]
21. Yang, X.; Wen, G.; Sun, H.; Cao, J.; Wang, B.; Dai, L.; Lu, J. Development and application of simulation experimental system for impact dynamic effect and disaster-causing characteristics of coal and gas outburst. *J. China Coal Soc.* **2023**, *48*, 3731–3749. [CrossRef]
22. Liu, T. Numerical simulation on characteristics of impinging air flow propagationand CO formation in lignite explosion. *Explos. Shock Waves* **2019**, *39*, 105401. [CrossRef]
23. Zhou, B.; Xu, J.; Yan, F.; Peng, S.; Gao, Y.; Li, Q.; Cheng, L. Effects of gas pressure on dynamic response of two-phase flow for coal–gas outburst. *Powder Technol.* **2021**, *377*, 55–69. [CrossRef]
24. Tu, S.; Dou, F.; Mo, Z.; Wang, F.; Yuan, Y. Strata control technology of the fully mechanized face in shallow coal seam close to the above room and pillar gob. *J. China Coal Soc.* **2011**, *36*, 366–370.
25. Wang, G.; Cheng, W.; Xie, J. Field test research on two-dimensional gas concentration and temperature distribution in the goaf of fully mechanized caving face. *Procedia Eng.* **2012**, *43*, 478–483. [CrossRef]